Chapter 9

Electron Tunneling Kinetics in Cytochrome cb_{562}

9.1 Introduction

In this chapter, we probe electron tunneling rates in cytochrome cb_{562}. We are interested in improving our fundamental understanding of electron tunneling pathways in proteins. The acquired knowledge can be applied to the design of protein-based electronic devices [83]. For example, to take advantage of the excellent electrocatalytic properties of enzymes in fuel cells, the electronic coupling between the protein's active site and the electrode surface must be optimized [84].

9.1.1 Long-Range Electron Transfer in Proteins

Electron transfer in proteins is a nonadiabatic process that occurs over distances as far as 30 Å through quantum mechanical tunneling. The key relationship that describes electron transfer processes is the Marcus equation [85]:

$$k_{\text{ET}} = \sqrt{\frac{4\pi^3}{h^2\lambda RT}} \times H_{AB}^2 \times \exp\left\{-\frac{(\Delta G^\circ + \lambda)^2}{4\lambda RT}\right\} \tag{9.1}$$

where H_{AB} is the electronic coupling matrix element, $-\Delta G^\circ$ is the reaction driving force, and λ is the reorganization energy. H_{AB} exhibits an exponential dependence on distance, represented by β, that becomes particularly relevant in long-range reactions [86].

The exponential decay constant β, which depends on the medium between the two redox-active sites, was probed in activationless systems of different media, including proteins [87, 32]. Two theories are used to explain the β values for different materials, the superexchange model [88] and the uniform barrier model [89]. The tunneling timetable in Figure 9.1 illustrates the distance dependence of electron transfer rates for various proteins. Protein tunneling times are scattered around a β of 1.1 Å^{-1}, most similar to saturated hydrocarbons (1.0 Å^{-1}) and toluene (1.18–1.28 Å^{-1}). The scatter in the data for the α-helical proteins suggests that proteins are not uniform media, which is in fact the case.

Beratan, Onuchic, and co-workers derived a superexchange model for electron transfer in proteins that accounts for the structural complexity of proteins [90, 91, 92]. In this tunneling-pathway model, coupling pathways are broken down into covalent bonds, hydrogen bonds, through-space jumps, and van der Waals interactions, which are combined to create a pathway-specific β value.

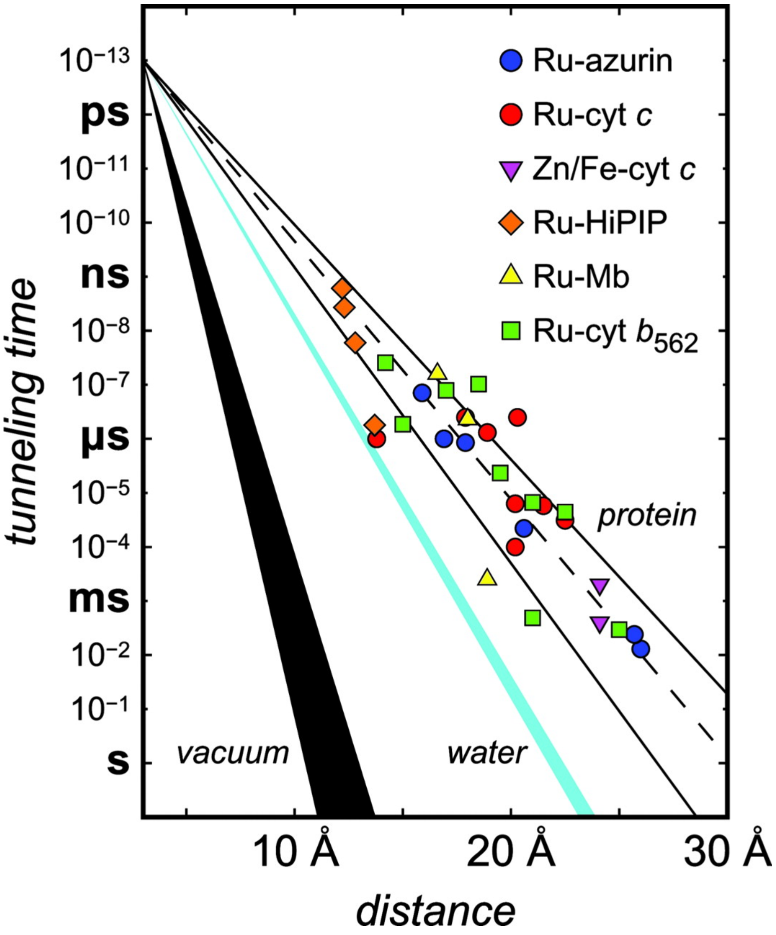

Figure 9.1: Tunneling timetable for proteins. The solid lines illustrate tunneling-pathway predictions for coupling along β-strands (β= 1.0 Å^{-1}) and α-helices (β= 1.3 Å^{-1}). Ru-modified cytochrome b_{562} time constants are represented by green squares. Duplicated with permission from Gray et al. [32].

9.1.2 Electron Tunneling in Cytochromes b_{562} and cb_{562}

The Gray Group previously characterized the electron tunneling rates through the α-helices of Ru-modified cytochrome b_{562} (Figure 9.1) [93, 94]. The data are not well described by a single β value. Prytkova, Kurnikov, and Beratan modeled the electron tunneling pathways in cytochrome cb_{562} and were able to fit seven of the nine variants to a β of 1.3 Å^{-1} [95]. They found that, in the seven variants, electrons tunneled through the heme edge via multiple accessible pathways. The averaging of multiple coupling pathways led to the insensitivity of rates to structure.

In contrast, tunneling rates were slower for the other two variants (His12 and His73) where electrons tunneled to the Fe along a single, dominant pathway through an axial ligand. Thus, dominant pathways are especially sensitive to the protein structural features along the pathway. By this line of reasoning, structural changes to the heme that cause changes in the tunneling mechanism should also alter tunneling rates, even though the distance is conserved.

The protein was modified to cytochrome cb_{562} by introducing covalent linkages from the heme porphyrin to the protein backbone, as depicted in Figure 3.13 and described in Chapter 3. In this modified protein, the heme is coordinated more rigidly to the protein than in the *b*-type cytochrome, where the heme is bound only by axial ligations to a methionine and a histidine residue. We investigate the effects of these changes to the protein structure, i.e., increased rigidity and potential new equatorial tunneling pathways through the covalent linkages, on electron transfer rates in a series of Ru-modified variants (Figure 9.2).

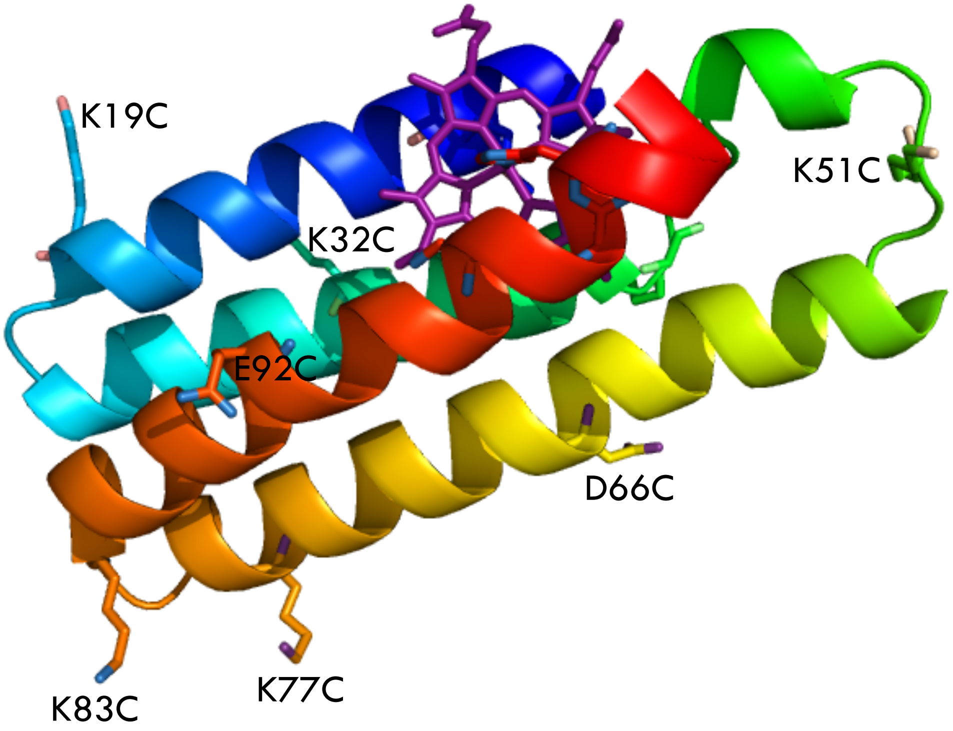

Figure 9.2: We measure Ru–heme electron tunneling rates in cytochrome *cb*$_{562}$. [Ru(bpy)$_2$(IA-phen)]$^{2+}$ is coupled covalently to surface-exposed cysteines, distributed throughout the protein in single-mutation variants. We have confirmed by circular dichroism and UV-visible spectroscopy that the cysteine mutations and Ru complex do not alter the structure of the protein (section 4.3).

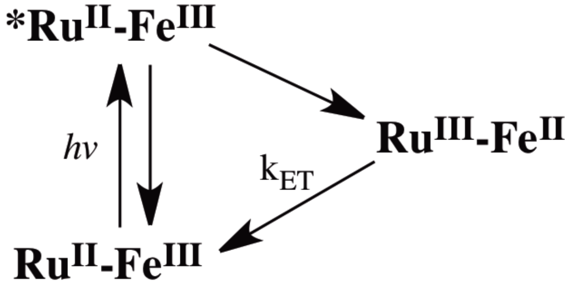

Figure 9.3: Photochemistry of the electron transfer reaction. The back electron transfer rate constant is designated k_{ET}.

9.1.3 Photochemical Triggers

We trigger electron transfer photochemically (Figure 9.3). The Ru label is photoexcited at 480 nm, forming the highly reducing species $*Ru^{II}$. This excited state species can reduce the heme Fe^{III}. For electron transfer to occur, it must be faster than the rate of $*Ru^{II}$ relaxation, or luminescence. We observe the forward ($*Ru^{II}$-Fe^{III}) and back (Fe^{II}-Ru^{III}) electron transfer steps and report the back electron transfer rate constants (k_{ET}).

In studies of cytochrome b_{562}, single-histidine variants were labeled with $[Ru(bpy)_2(imidazole)(His\text{-}imidazole)]^{2+}$. We present data for cytochrome cb_{562} with a different photosensitizer ($[Ru(bpy)_2(IA\text{-}phen)]^{2+}$, Figure 1.7) that is bound covalently to cysteine residues by a flexible linker. The advantages of this new Ru photosensitizer are that it has a longer lifetime (800 ns versus 70 ns), cysteine variants may now be labeled, and the labeling reaction is simpler. A major disadvantage is the uncertainty in the Ru–Fe distance introduced by the flexible linker. A collaboration is underway with Tatiana Prytkova to model the tunneling pathways and the corresponding distance.

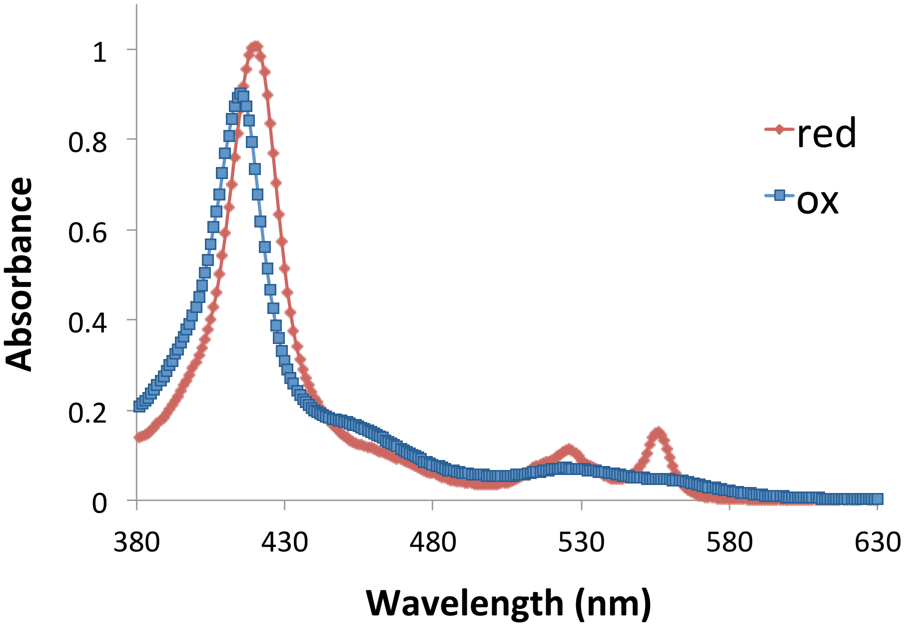

Figure 9.4: Absorption spectrum of oxidized and reduced cytochrome *cb*$_{562}$. Upon reduction of Ru-ferricytochrome *cb*$_{562}$ at pH 7, the Soret maximum shifts from 415 nm to 420 nm.

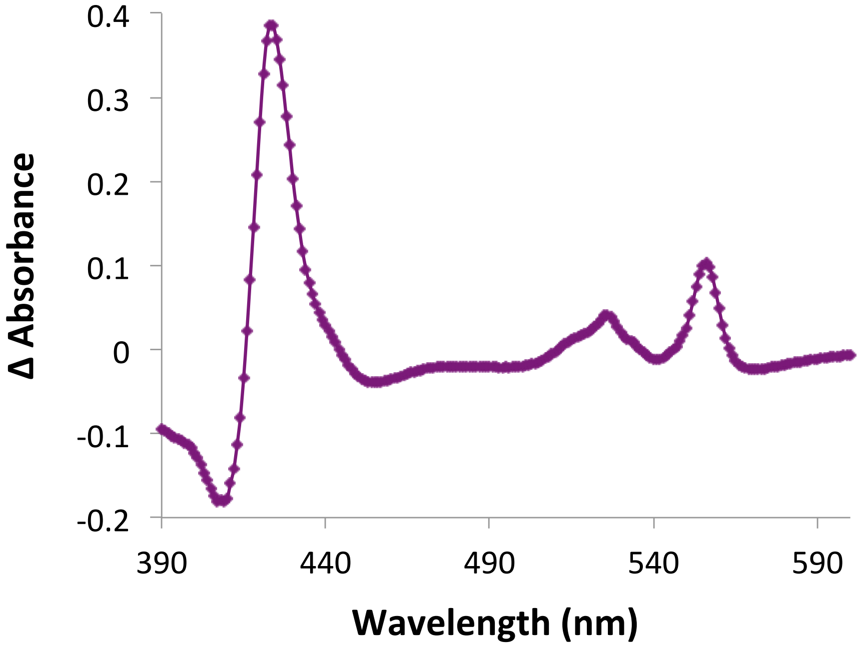

Figure 9.5: The difference spectrum between oxidized and reduced cytochrome *cb*$_{562}$ exhibits maximal absorbance changes at 409 and 424 nm. We monitor transient absorption kinetics at these wavelengths.

9.2 Difference Absorption Spectrum

To measure electron tunneling rates, the transient species $\mathrm{Fe^{II}}$ is monitored at wavelengths that show maximal absorbance changes. The Soret peak of cytochrome cb_{562} red shifts upon reduction (Figure 9.4). The difference spectrum of the oxidized and reduced protein indicates that the largest absorbance changes following reduction occur at 409 and 424 nm (Figure 9.5).

9.3 Kinetic Data

The quenching of the $^{*}\mathrm{Ru^{II}}$ luminescence ($k = 1.30 \pm 0.05 \times 10^{6}\ \mathrm{s^{-1}}$ at pH 7) and the corresponding formation of $\mathrm{Fe^{II}}$ are indicative of electron transfer. Luminescence decays for the variants are depicted in Figure 9.6, and the rate constants from exponential fits are summarized in Table 9.1. Luminescence decay rates are consistent with exponential fits of the forward electron transfer step, measured by transient absorption.

Transient absorption signals for the Ru-variants are presented in Figures 9.7–9.12. The data fit to biexponential functions where the rate constants correspond to the forward and back electron transfer steps. (The large difference in forward and back rates for Ru66 complicated fits to a biexponential function; instead, the back electron transfer step was fit to a monoexponential function.) The back electron transfer rate constants are summarized in Table 9.1. Electron transfer is not observed for Ru77 and Ru83; the signal decay fits to a single exponential that

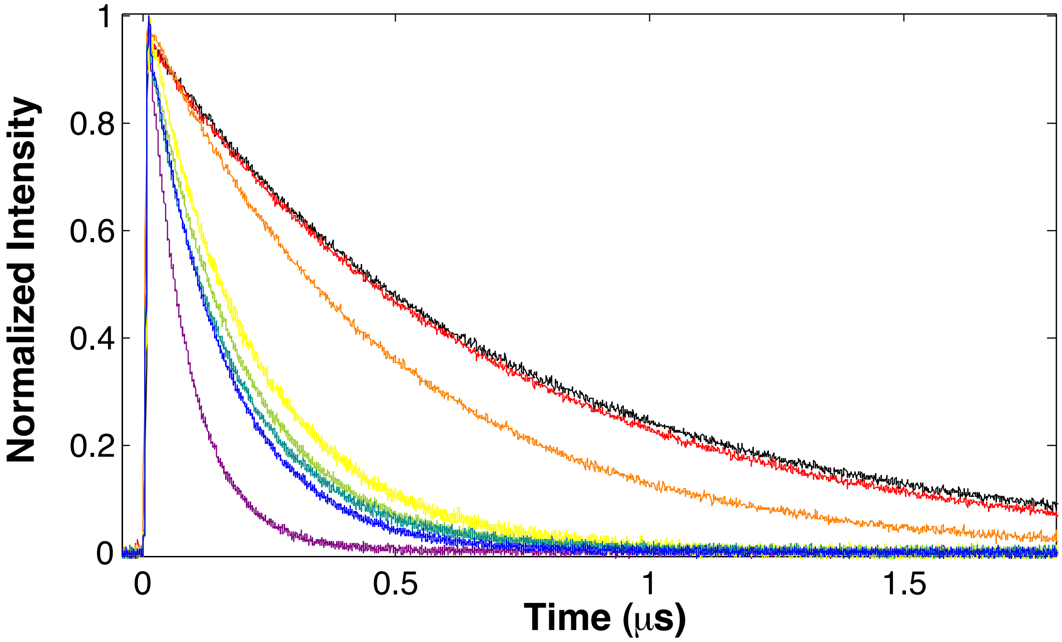

Figure 9.6: Luminescence decays of Ru-modified cytochrome *cb*$_{562}$ variants and free label. With increasing decay times—Ru32 (violet), Ru92 (blue), Ru51 (teal), Ru19 (green), Ru66 (yellow), Ru77 (orange), Ru83 (red), and label (black).

corresponds to the luminescence rate. Electron transfer is likely too slow at these distances to be competitive with the relaxation of *Ru^{II} by luminescence.

At 424 and 409 nm, *Ru^{II} has a smaller absorbance than Ru^{II} and causes a bleach at time zero. As Fe^{II} has a larger absorbance than Fe^{III} at 424 nm, formation of Fe^{II} is observed as a growth in intensity, so that the signal crosses the baseline in the first kinetic process. In contrast, at 409 nm, Fe^{II} has a negative change in absorbance and is observed following the decay of *Ru^{II} in the first kinetic process. During the second kinetic process, the curve decays to the baseline as the reactant (Ru^{II}-Fe^{III}) is recreated.

Transient ruthenium species can be monitored at 460 nm (Figure 9.11), where the difference in the absorbance of Fe^{III} and Fe^{II} is small (Figure 9.5). We fit

Table 9.1: Luminescence and electron tunneling back rate constants in Ru-modified cytochrome cb_{562} variants.

Variant	Distance (Å)[†]	Luminescence (s^{-1})	k_{ET} (s^{-1})/424 nm	k_{ET} (s^{-1})/409 nm
Ru32	21.3	1.15 (± 0.05) x 10^7	4.1 (± 0.5) x 10^6	2.8 (± 0.3) x 10^6
Ru92	21.3	6.40 (± 0.07) x 10^6	3.7 (± 0.1) x 10^5	3.7 (± 0.1) x 10^5
Ru51	22.2	5.7 (± 0.1) x 10^6	2.7 (± 0.3) x 10^5	3.0 (± 0.3) x 10^5
Ru19	24.8	5.35 (± 0.07) x 10^6	2.8 (± 0.3) x 10^5	2.6 (± 0.1) x 10^5
Ru66	19.9	4.6 (± 0.3) x 10^6	2.3 (± 0.4) x 10^3	2.3 (± 0.4) x 10^3
Ru77	29.4	2.0 (± 0.1) x 10^6	not observed	not observed
Ru83	33.0	1.6 (± 0.2) x 10^6	not observed	not observed

[†] C_γ–Fe distance measured in crystal structure (PDB 2BC5) + 5 Å (approximation).

the forward ($^*Ru^{II} \rightarrow Ru^{III}$) and back ($Ru^{III} \rightarrow Ru^{II}$) electron transfer kinetics with biexponential functions. The decay of $^*Ru^{II}$ was also monitored at 370 nm (Figure 9.11).

Based on the distance estimates, the rate constants for Ru32 and Ru66 noticeably diverge from the distance dependence. Tunneling to Ru32 is an order of magnitude faster than to Ru92, although it is estimated to be the same distance from the heme. Ru66 is several angstroms closer to the heme, but tunneling is two orders of magnitude slower. As discussed, there is uncertainty in the distance measurement; the estimate is based on the cysteine C_γ–Fe distance, however, the Ru linker could face toward or away from the heme. After obtaining distances from the calculations, we will determine a β for tunneling in cytochrome cb_{562}, identify the outliers, and compare the tunneling pathways.

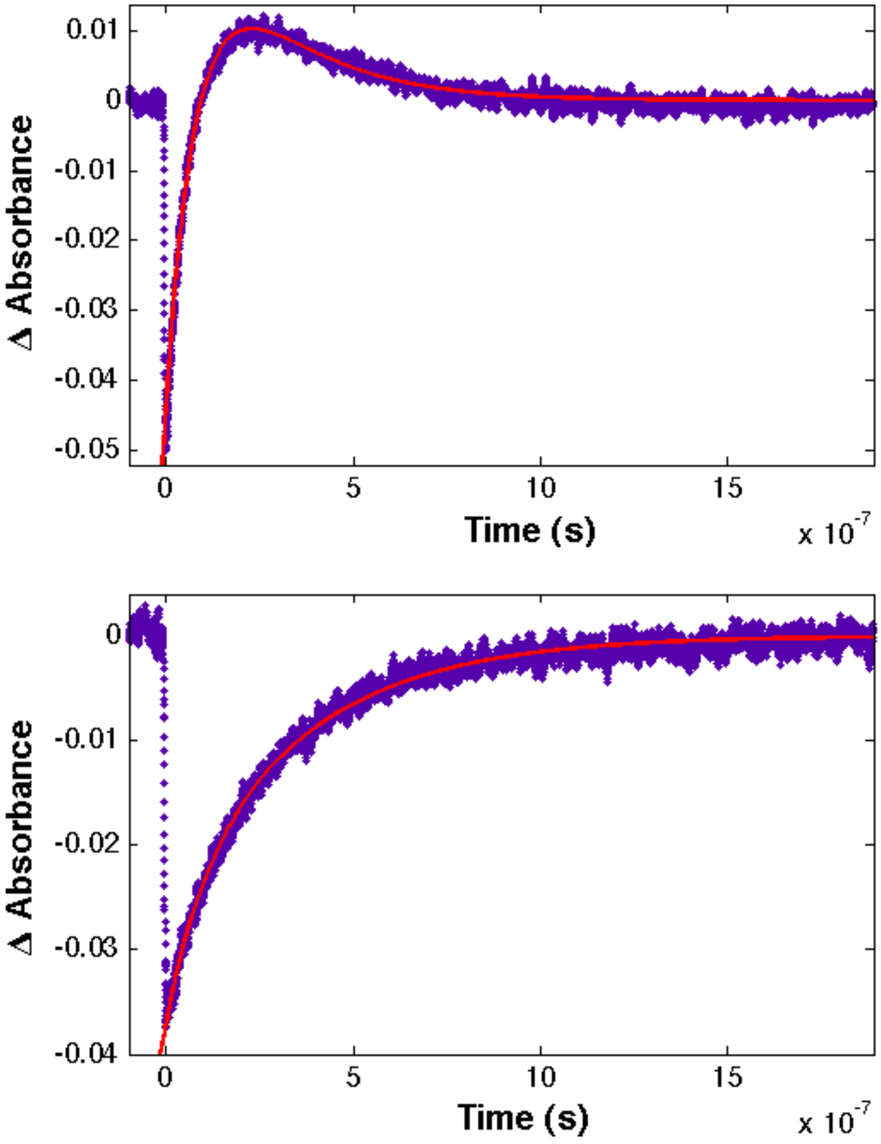

Figure 9.7: Transient absorption spectra of Ru32 at 424 nm (upper) and 409 nm (lower).

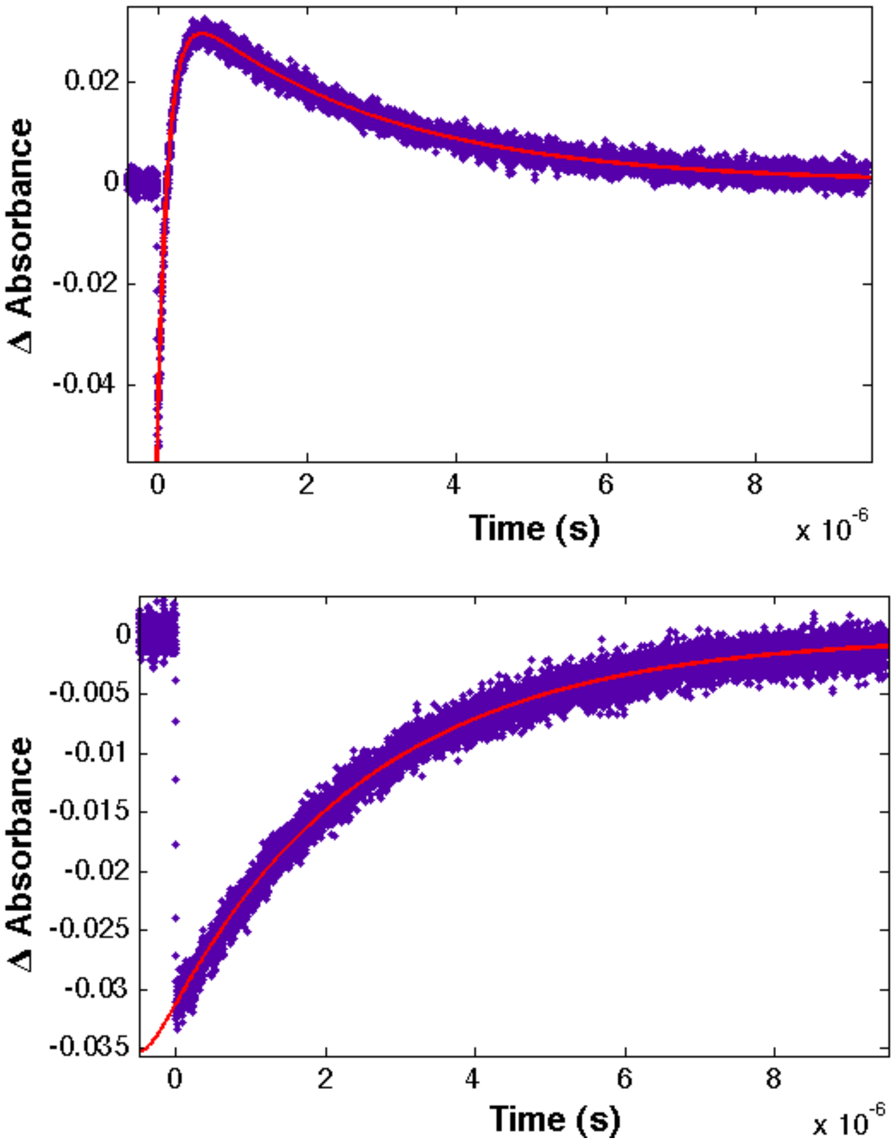

Figure 9.8: Transient absorption spectra of Ru92 at 424 nm (upper) and 409 nm (lower).

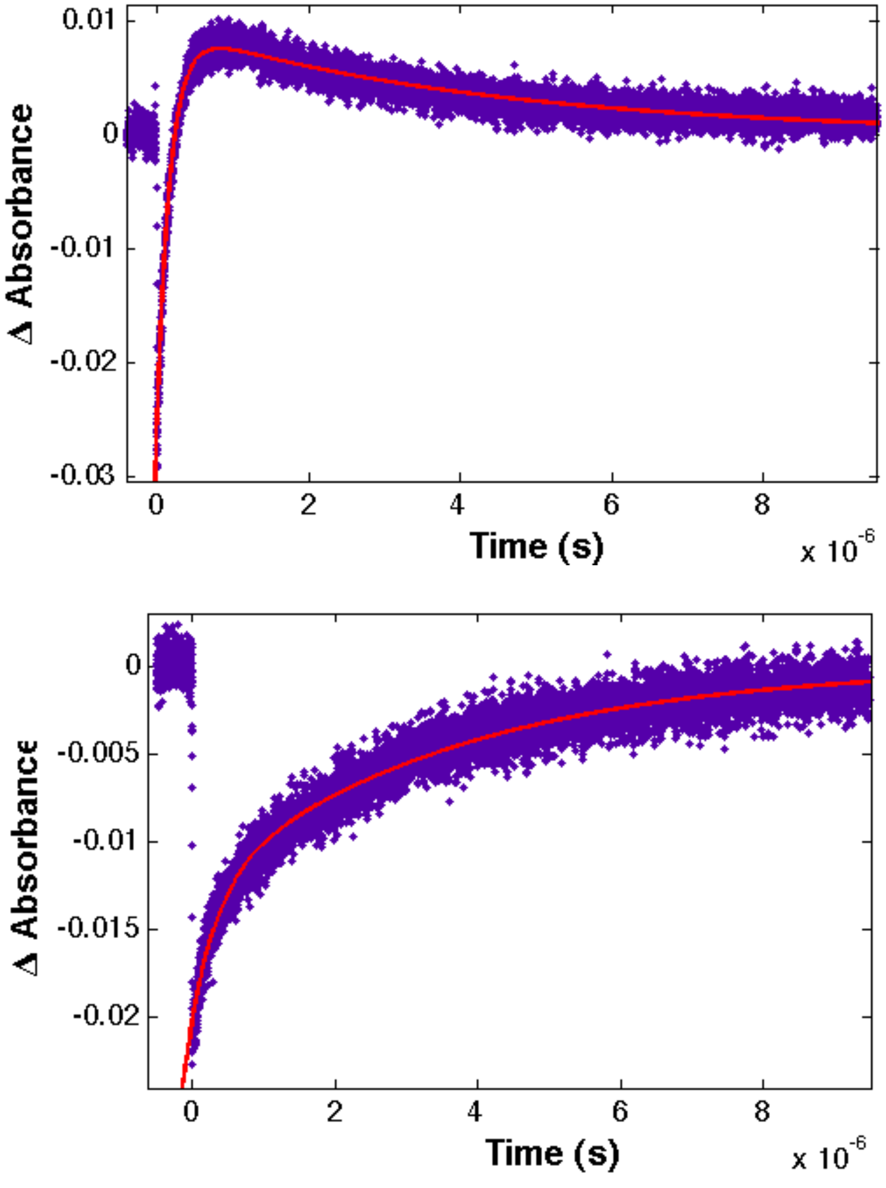

Figure 9.9: Transient absorption spectra of Ru51 at 424 nm (upper) and 409 nm (lower).

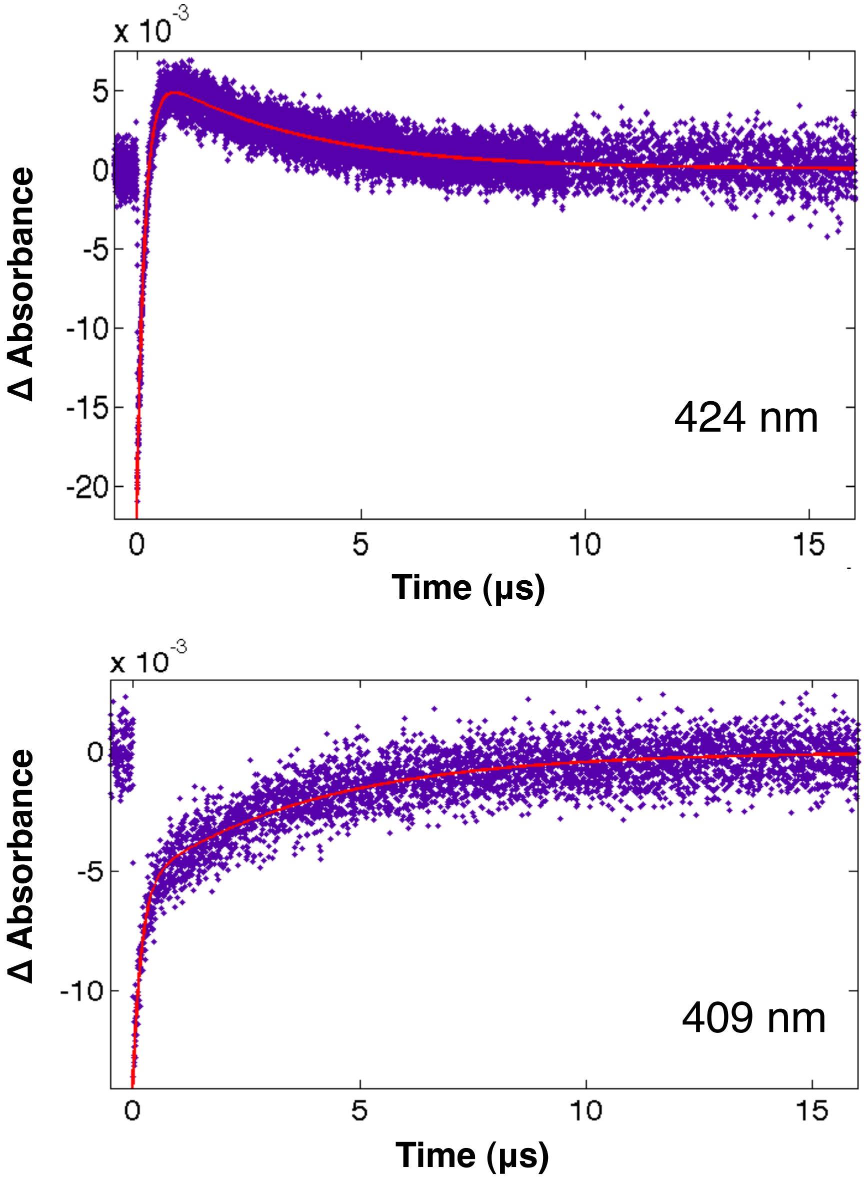

Figure 9.10: Transient absorption spectra of Ru19 at 424 nm (upper) and 409 nm (lower).

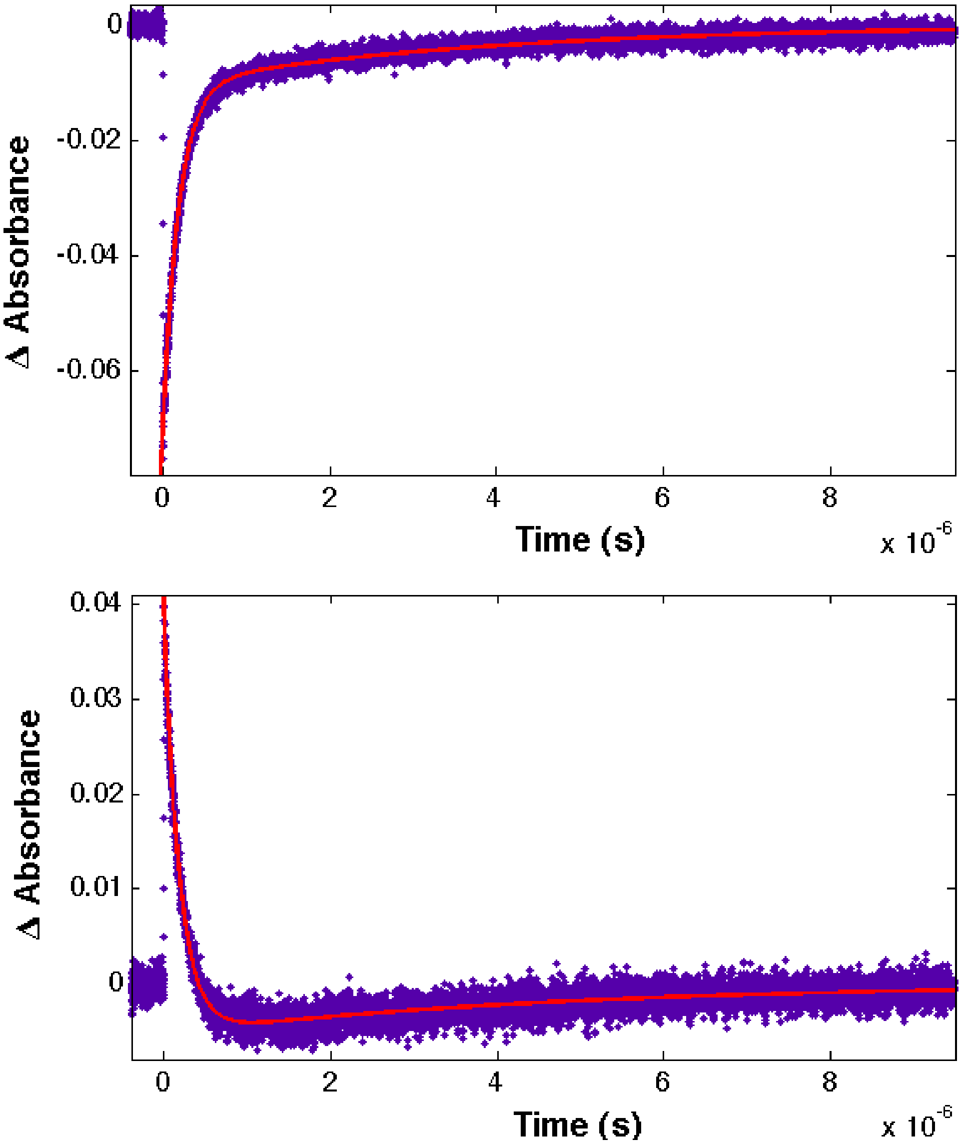

Figure 9.11: Representative transient absorption spectra at 460 nm (upper) and 370 nm (lower), Ru19.

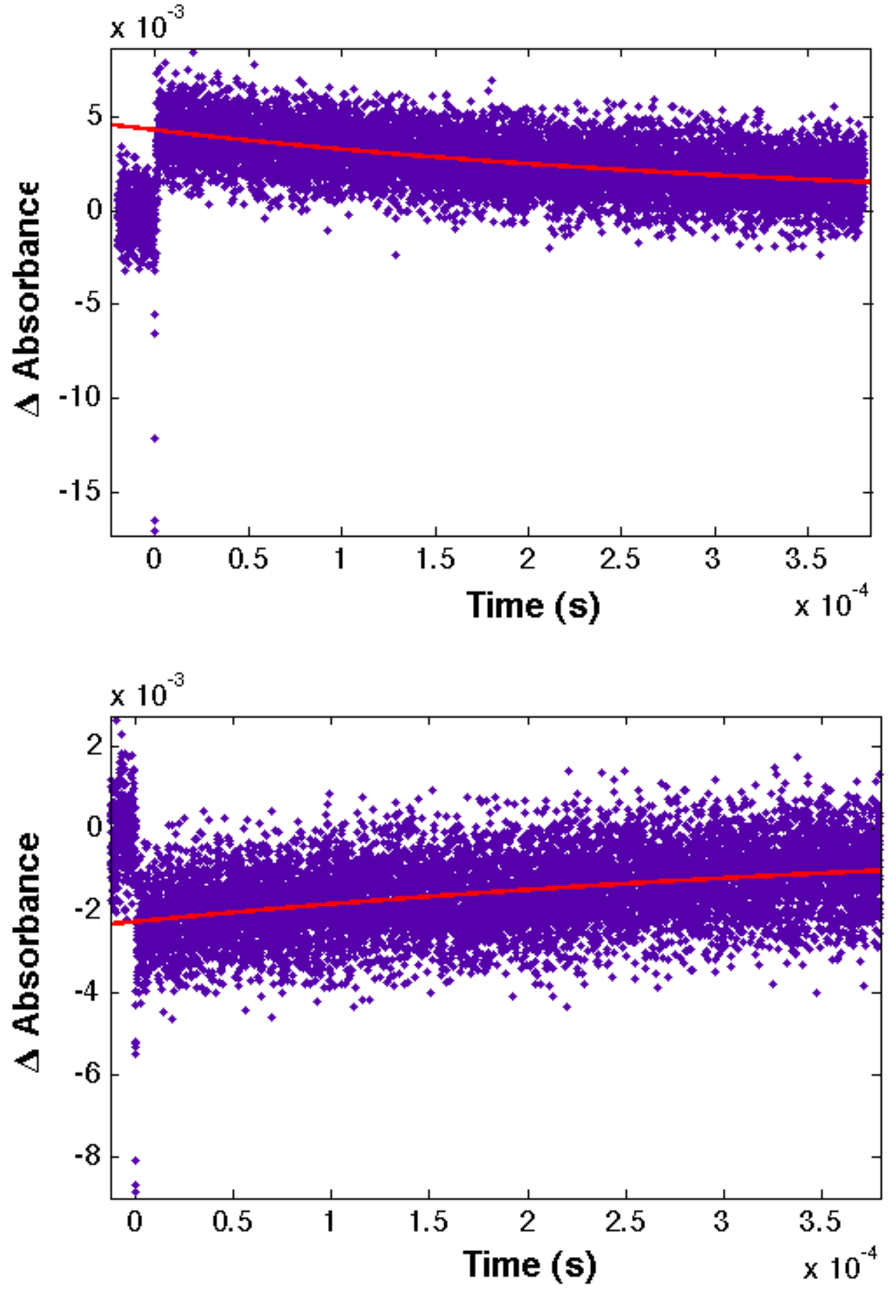

Figure 9.12: Transient absorption spectra of Ru66 at 424 nm (upper) and 409 nm (lower).

Experiments are underway to compare electron tunneling rates in cytochromes cb_{562} and b_{562} in corresponding variants—K19C, K19H, E92C, and E92H. Preliminary results indicate no change in the tunneling rates in Ru-Cys19 with the structural changes to the heme. Tunneling pathways are likely unchanged for Ru-Cys19 or Ru-His19 variants on helix 1 as the covalent porphyrin linkages are on opposite edge of the heme. In contrast, tunneling between residue 92 on helix 4, the covalently linked helix, and the heme could involve the engineered covalent porphyrin linkages. A significant change in the rate would suggest changes in the tunneling mechanism, from multiple pathways to a single dominant pathway.

9.4 Conclusions

With approximations of the Ru–Fe distance, we identify two outliers from the exponential dependence of rate constants on tunneling distance—position 32 on helix 2, which is very fast, and position 66 on helix 3, which is significantly slower than expected. Calculations will provide more accurate distances and insight into tunneling pathways. Additional variants will allow for direct comparisons of tunneling pathways in cytochromes cb_{562} and b_{562}.

9.5 Acknowledgments

I would like to thank Heather Williamson for experimental advice when I started this project and helpful discussions throughout our time working together. I would also like to acknowledge Tatiana Prytkova (Chapman University), a collaborator who is tackling this challenging problem with computational methods.